TUDelft

Delft University of Technology

Realizing the Potential of RF-Sputtered Hydrogenated Fluorine-Doped Indium Oxide as an Electrode Material for Ultrathin SiO x/Poly-Si Passivating Contacts

Han, Can; Yang, Guangtao; Montes, Ana; Procel, Paul; Mazzarella, Luana; Zhao, Yifeng; Eijt, Stephan; Schut, Henk; Zhang, Xiaodan; Zeman, Miro

Important note
To cite this publication, please use the final published version (if applicable).
Please check the document version above.

ACS APPLIED ENERGY MATERIALS

Article

Realizing the Potential of RF-Sputtered Hydrogenated Fluorine-Doped Indium Oxide as an Electrode Material for Ultrathin SiO$_x$/Poly-Si Passivating Contacts

Can Han,* Guangtao Yang, Ana Montes, Paul Procel, Luana Mazzarella, Yifeng Zhao, Stephan Eijt, Henk Schut, Xiaodan Zhang, Miro Zeman, and Olindo Isabella*

Read Online

ACCESS | Metrics & More | Article Recommendations | Supporting Information

ABSTRACT: In high-efficiency silicon solar cells featuring carrier-selective passivating contacts based on ultrathin SiO$_x$/poly-Si, the appropriate implementation of transparent conductive oxide (TCO) layers is of vital importance. Considerable deterioration in passivation quality occurs for thin poly-Si-based devices owing to the sputtering damage during TCO deposition. Curing treatment at temperatures above 350 °C can recover such degradation, whereas the opto-electrical properties of the TCO are affected as well, and the carrier transport at the poly-Si/TCO contact is widely reported to degrade severely in such a procedure. Here, we propose straightforward approaches, post-deposition annealing at 400 °C in nitrogen, hydrogen, or air ambience, are proposed to tailor material properties of high-mobility hydrogenated fluorine-doped indium oxide (IFO:H) film. Structural, morphological, and opto-electrical properties of the IFO:H films are investigated as well as their inherent electron scattering and doping mechanisms. Hydrogen annealing treatment proves to be the most promising strategy. The resulting layer exhibits both optimal opto-electrical properties (carrier density = 1.5×10^{20} cm^{-3}, electron mobility = 108 cm^2 V^{-1} s^{-1}, and resistivity = 3.9×10^{-4} Ω cm) and remarkably low contact resistivities (∼20 mΩ cm^2 for both n- and p-contacts) in poly-Si solar cells. Even though the presented cells are limited by the metallization step, the obtained IFO:H-base solar cell show an efficiency improvement from 20.1 to 20.6% after specific hydrogen treatment, demonstrating the potential of material manipulation and contact engineering strategy in high-efficiency photovoltaic devices endowed with TCOs.

KEYWORDS: hydrogenated fluorine-doped indium oxide (IFO:H), transparent conductive oxide (TCO), carrier-selective passivating contacts, ultrathin SiO$_x$/poly-Si passivating contacts, hydrogen annealing
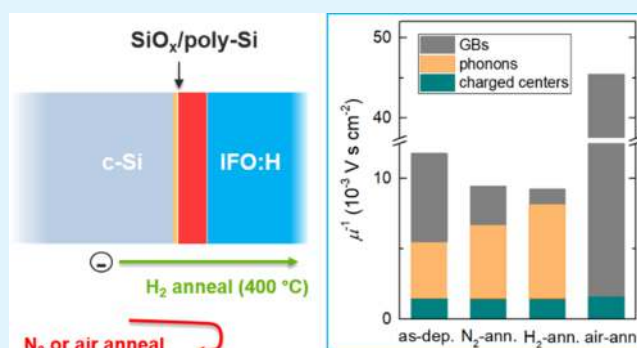
1. INTRODUCTION

In efficiency-driven photovoltaic (PV) industry, the market-dominating crystalline silicon (c-Si) technology evolved from the traditional aluminum back surface field (Al-BSF) cell to passivated emitter rear contact (PERC) cell architecture, resulting, at the production level, in power conversion efficiency (PCE) well above 20%.[1] However, PERC cells feature localized metal-silicon contacts, which still suffer from high recombination.[2] To push forward the practical PCE, c-Si solar cells featuring carrier-selective passivating contacts (CSPCs) are developed, which have demonstrated viable novel cell concepts with PCE well above 25%.[3] Such CSPCs enable low contact resistance and good passivation quality of the c-Si surface, thus appreciably enhancing the contact selectivity as compared to conventional diffused junctions.[3] Applying CSPCs based on ultrathin SiO$_x$/poly-Si in front/back-contacted (FBC) silicon solar cells remains to be further exploited due to the significant optical loss caused by parasitic

absorptive doped layers.[4,5] In fact, in FBC c-Si solar cells featuring ultrathin SiO$_x$/poly-Si passivating contacts at both front and rear sides (so-called poly-Si solar cell), parasitically absorptive poly-Si layers cannot be deposited thick enough to provide sufficient lateral conductivity for the current transport toward the metal grid. To solve this dilemma, transparent conductive oxide (TCO) layers on top of a thin poly-Si layer ensure the required lateral conductivity and constitute a more transparent front window.[1,6] However, commonly used sputtering technology is known to degrade the passivation quality of thin poly-Si contacts.[4] Owing to the high thermal
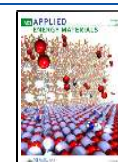
stability of poly-Si contacts, an effective curing can be achieved at ~350 °C to restore the passivation.[4] Nevertheless, carrier transport at the poly-Si/TCO contact is widely reported to degrade severely for temperatures above 250 °C,[4] likely due to the formation of an interfacial SiO_x with oxygen effusing from the TCO.[4,6−9] Such drawbacks in carrier transport need to be solved to achieve a high PCE in FBC poly-Si solar cells.

As for the TCO alternatives, it is well known that there is a trade-off between optical transparency and electrical conductivity in TCO material design.[10] High carrier mobility (μ) is generally required for the TCO films used in PV applications to ensure a low sheet resistance (R_{sh}) at a moderate carrier density (N_e) level, providing high transparency with reduced free carrier absorption (FCA) in the visible and near-infrared regions (NIR).[10,11] To this end, various doped TCOs were developed over the past decades, mostly with cationic metallic dopants such as Ce, Zn, Ti, Zr, W, Mo, Hf, etc.[10,12−15] (with or without hydrogen as co-dopant), in which Mo,[13] Ce,[16] and Zr[14] have been identified as resonant dopants, i.e., they provide donor states without perturbing the conduction band, thus allowing high electron mobilities. TCOs of In_2O_3 doped with Ce[4] and Zr[11] have been shown to have very low FCA in the absorption range of c-Si solar cells. Apart from this, anionic dopants such as fluorine provide another attractive approach in producing TCO films with relatively high lateral conductivity in conjunction with low optical absorption loss.[12,17,18] In our previous work,[12] we developed a high-μ hydrogenated fluorine-doped indium oxide (IFO:H) film, in which fluorine and hydrogen act as co-dopants in a bixbyite In_2O_3 structure. Specifically, fluorine dopants enhance the electrical properties of In_2O_3 film via (i) substituting for oxygen atoms thus generating free electron carriers, (ii) occupying oxygen vacancy sites thus eliminating electron trap sites, (iii) lowering the transport barrier at the grain boundaries, while the introduction of hydrogen further enhances the electrical properties of the fluorine-doped In_2O_3 film by acting as shallow donors and passivating defects in the film. The application of the IFO:H film in different c-Si solar cells with passivating contacts has been demonstrated. For the low thermal-budget architecture such as silicon heterojunction solar cells, our IFO:H-based devices showed comparable fill factor (FF) as the ITO-based counterparts. In this sense, we might say that IFO:H outperforms its close relative hydrogen-doped indium oxide (IO:H), which has been reported to face FF losses in silicon heterojunction devices.[19,20] However, it remains elusive to realize the potential of the IFO:H film in high thermal-budget devices, especially due to the aforementioned carrier transport problem for poly-Si passivating contacts in a passivation restoring step. It has been reported that the electrical behavior of polycrystalline In_2O_3 from room temperature to 800 °C is influenced by impurities and oxygen vacancies (V_O) that act as donor states in degenerated TCO layers.[21−23] In addition, amphoteric hydrogen provides donor states in metal oxide, inducing alteration and changing the opto-electrical properties in the host matrix.[20,23−25] On the other hand, in the case of semiconductor application with Si/SiO_2 interface, atomic hydrogen is found to simultaneously passivate and depassivate silicon dangling bonds,[26] resulting in different passivation qualities at the device level. Furthermore, hydrogen effused from TCO could help to passivate interfacial defects.[27] Therefore, engineering these defect states is of vital importance in tailoring both the opto-electrical properties of the TCO and contact at specific poly-Si polarity.

In this study, we demonstrated different straightforward approaches to alter the opto-electrical properties of the IFO:H film. Particularly, we examined the influence of post-deposition annealing (PDA) treatment in different gaseous ambiences on the IFO:H structure, morphology, and opto-electrical properties. Corresponding inherent electron scattering mechanisms were also elucidated. We found that a specific PDA treatment provides the most promising strategy to tailor material's properties while retaining a good contact for carrier transport across poly-Si/TCO contact. As a proof of that, FBC poly-Si solar cells were then manufactured and those that underwent the PDA treatment exhibited increased fill factor (FF).

2. EXPERIMENTAL SECTION

2.1. TCO Deposition and Post-deposition Annealing (PDA) Treatments. TCO films were prepared using RF magnetron sputtering. The IFO:H film was sputtered from a commercially available fluorine-doped In_2O_3 target from Advanced Nano Products Co., Ltd. The process parameters were chosen for optimum opto-electrical properties of the as-deposited films, which were as follows: Ar flow = 50 sccm, substrate temperature = 100 °C, chamber pressure = 2.50×10^{-3} Pa, water vapor partial pressure = 1.6×10^{-5} Pa, and power density = ~1.8 W/cm². These conditions yielded a IFO:H deposition rate of ~6.0 nm/min. The F/In atomic ratio in the film is ~17% from X-ray photoelectron spectroscopy (XPS) analysis.[12] For comparison purpose, ITO films were deposited from a target containing 90 wt % of In_2O_3 and 10 wt % of SnO_2 with Ar flow = 50 sccm, substrate temperature = 100 °C, chamber pressure = 2.20×10^{-3} Pa, and power density = ~1.8 W/cm². The ITO deposition rate was ~6.5 nm/min. Before deposition, the targets were usually pre-sputtered for 5 min to remove any contaminants and eliminate any differential sputtering effects. During the deposition, a rotation of the sample holder of 5 rpm was maintained to ensure the uniformity of the TCO films. Samples were subject to different post-deposition annealing (PDA) treatments as tabulated in Table 1. We note that in

Table 1. Post-deposition Annealing (PDA) Treatments on Different IFO:H Samples

sample	temperature (°C)	ambience	[a] pressure (Pa)	[b] duration (min)
as-dep.				
N$_2$-ann.	400	pure nitrogen	50	10
H$_2$-ann.	400	pure hydrogen	50	60
air-ann.	400	air	atmospheric	10

[a]We did annealing tests in different tools, such as rapid thermal annealer in Kavli nanolab, Mapper annealing tube, and different multi-chamber PECVD systems in EKL lab. The results from the same ambience showed similarity, even though the pressure control levels were different among the annealing tools. The results from Cascade PECVD were used in this article for a better gas pressure controllability, and 50 Pa was used to keep a constant oxygen-deficient environment in the annealing treatment. [b]Hydrogen annealing with durations of 10 min up to 30 min did not cause observable changes in the opto-electrical properties of the IFO:H film, and the duration of 60 min gave comparable improvements with the N$_2$-ann. sample in electrical properties; thus, the duration of the H$_2$-ann. sample was set to be 60 min. An even longer hydrogen annealing time was deemed not industrially appealing.

our various annealing tests regarding the single TCO layer, our IFO:H films were stable up to 300 °C in N$_2$, H$_2$, and air ambiences, and annealing temperature above 400 °C facilitated considerable changes in electrical properties (a duration of 10 min was used in the annealing tests, "stable" means that the sheet resistance change upon annealing is within 5% compared to the as-deposited film). To avoid overheating of our poly-Si cell precursors, 400 °C was chosen to
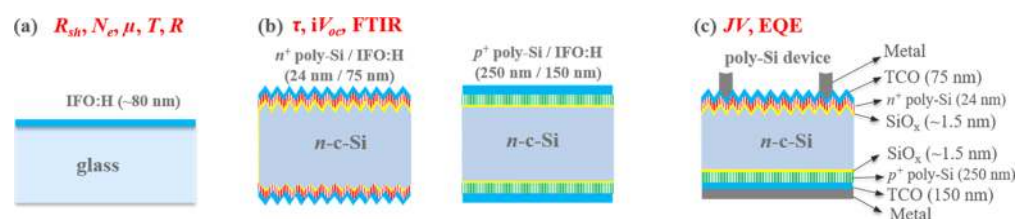
Figure 1. Overview of (a, b) fabricated test structures and (c) poly-Si solar cell with corresponding measured parameters.

stimulate opto-electrical properties change in TCO and to maintain the passivation quality at the Si/SiO$_2$ interface.[26,28]

2.2. Material Characterization. Approximately 80 nm-thick IFO:H thin films were deposited on Corning glasses substrates (Figure 1a) unless otherwise specified. Their opto-electrical properties were evaluated with a Hall effect measurement setup HMS-5000 (ECOPIA CORP) and a spectroscopic ellipsometry (SE) M-2000DI system (J.A. Woollam Co., Inc.). In Hall measurements, carrier density (N_e), carrier mobility (μ_{hall}), and resistivity (ρ) are determined, in which the Hall scattering factor is assumed to be unity in our degenerate TCO samples.[29] Apart from room temperature measurements, temperature dependence of the electrical properties was also evaluated from 200 to 350 K. First, the measured film was cooled down to 200 K with liquid nitrogen, and the electrical properties were measured during heating up to 350 K.[23] SE instead was used to determine bulk thickness (d_b), surface roughness (d_s), optical mobility (μ_{opt}), Urbach energy (E_U), and complex refractive index of the films. To prevent backside reflections with transparent substrates, cloudy tape was applied on the backside of the glass substrates.[30] The measured photon energy range was 0.75−6.5 eV, while the incidence angles were 55°, 60°, 65°, and 70°. The spectra showed similar features with different angle variations on one sample. The data from 70° were selected for analysis due to its ideal graphing depolarization conditions near zero, which indicates that little light is reflected from the backside into the detector. For the SE analysis, the dielectric function of the TCO film was considered to be homogeneous in depth and modeled by a combination of a Cody−Lorentz oscillator and a Drude oscillator to account for the absorption across the optical band gap in ultraviolet (UV) range and the free carrier absorption (FCA) in the near infrared (NIR) part of the spectrum, respectively.[23,31] Fixed values of $\varepsilon_\infty = 1$ was used in the fitting.[32] By assuming the effective electron mass $m^* = 0.30\ m_e$ and $N_{opt} = N_e$ from Hall measurements,[29,32−34] μ_{opt} can be obtained according to $\mu_{opt} = e\tau_{opt}/m^*$, in which e is the elementary charge and τ_{opt} is optical relaxation time from Drude fitting.[23,32] The effect of grain boundaries (GBs) can be evaluated from the ratio between μ_{Hall} and μ_{opt} because μ_{Hall} reflects all scattering phenomena, while μ_{opt} is not affected by GB scattering.[10,33] We note that uncertainties were included in the above calculation on μ_{opt} since m^* has been reported to change depending on N_e.[33,35]

The sheet resistance (R_{sh}) was measured by a four-point probe technique. According to the physical definition, $R_{sh} = \rho/d$, in which ρ is resistivity and d is the film thickness. Theoretically, the measured R_{sh} should be strictly consistent with the calculated data from Hall measurements and SE fitting. However, considering the differences in sample geometry and the contact issue (good ohmic contact between the probe and sample surface needs to be ensured in Hall measurement), the measured R_{sh} may not perfectly match related physical calculations, especially for not well-conductive samples (for instance, air-ann. film in this work).[36,37] In addition, the transmittance and reflectance spectra were obtained from a PerkinElmer Lambda 950 system. Additionally, the crystalline nature of the films was studied with the X-ray diffraction (XRD) technique. The XRD spectra were obtained on an XPERT-PRO diffractometer system with spinning stage (Spinner PW3064), and a Cu Kα radiation from the X-ray tube with normal focus was used (Cu Kα = 1.5406 Å). The characterization was operated at 45 kV with a 2θ scan range of 10−90°. Surface morphology scanning was carried out in NTEGRA PNL configurations from atomic force microscopy (AFM) mode at room

temperature. A high-accuracy non-contact composite probe consisting of a silicon body, polysilicon lever, and silicon high-resolution tip was utilized, whose resonant frequency is 120 ± 10% kHz. The scan area was set at 1 × 1 μm^2, and a topographic image consisted of 256 lines. Statistical roughness and grain analysis were conducted in NOVA program. Fourier transform infrared spectroscopy (FTIR) was used to evaluate interfacial silicon oxide formation on TCO-coated c-Si wafers. The measurements were performed in the NICOLET 5700 setup. First, we measured the FTIR spectra for all the four samples with one standard c-Si wafer piece as the reference sample, and the background spectra of the reference wafer was collected before each sample measurement. A KBr beam splitter and a transmission accessory were used. The measurements were done under dry nitrogen ambience with 1200 scans at a 4 cm^{-1} resolution. From this step, four measured spectra on four samples were obtained accordingly. Second, the measured spectra were analyzed by using the as-deposited IFO:H coated poly-Si stack as a baseline in the Omnic program. Based on such baseline correction, signals regarding the IFO:H/poly-Si interfacial silicon oxide, which represents the most distinct part among the samples, were enlarged and can be easily recognized.

Further, the presence of open-volume defects was studied by Doppler broadening positron annihilation spectroscopy (DB-PAS) using the mono-energetic low-energy positron beam VEP at Delft University of Technology.[38] A liquid nitrogen-cooled high-purity Ge (HPGe) detector with an energy resolution of 1.3 keV was utilized to determine the energy of the emitted positron-electron annihilation γ-rays. The line shape parameter S was calculated as the ratio of the central region ($|\Delta E| < 0.8$ keV) of the 511 keV annihilation γ-ray photopeak to the total area, and the wing parameter W was defined as the ratio of wing regions (2.1 keV < $|\Delta E| < 6.0$ keV) to the total area. The Doppler depth profiles collected in the range of 0.1−24 keV were fitted to extract S and W parameters of corresponding samples using the VEPFIT program.[38] The extracted thicknesses of IFO:H films from VEPFIT analysis were approximately 280, 280, 80, and 80 nm for as-dep., N$_2$-ann., H$_2$-ann., and air-ann. layers, respectively, providing a qualitative measure of their thicknesses. The VEPFIT analysis demonstrated that the two thicker layers consisted of a double layer, with a top ∼70 nm-thick IFO:H layer, consistent with the quantitative spectroscopic ellipsometry analysis.

2.3. Contact Study and Solar Cell Fabrication. In this work, n-type <100> oriented, 280 μm-thick, 1−5 Ω cm, double-side polished float zone (FZ) wafers were used as substrates unless otherwise specified. Figure 1b,c shows different test structures and solar cell schematic. After dipping the c-Si wafers into 0.55% HF for 4 min to remove the native oxide, the tunneling SiO$_x$ layer was formed by the method of nitric acid oxidation of silicon (NAOS).[39] In our case, we dipped the wafers in 68% HNO$_3$ bath for 1 h at room temperature. In order to obtain 250 nm-thick p^+ poly-Si layer for utilization at the rear side in our FBC poly-Si solar cells, a Varian Implanter E500HP was used to implant boron (B) atoms into the low-pressure chemical vapor deposition (LPCVD) intrinsic a-Si layer, with a fixed implantation energy of 5 keV and implantation dose of 5 × 10^{15} cm^{-2}. Afterward, an annealing step in N$_2$ and O$_2$ mixed ambience at 950 °C for 3 min was conducted to activate and drive in the dopants. The ramping rate for heating or cooling was 10 °C/min, and the doping level in the p-type poly-Si layer after activation and drive was around 1 × 10^{20} cm^{-3}.[39] To obtain the 24 nm-thick n^+ poly-Si layer on a textured surface for utilization at the front side in our FBC poly-

Si solar cells, we firsta textured the c-Si bulk in a mixture solution of TMAH and ALKA-TEX 8 from GP-Solar-GmbH followed by NAOS; then, intrinsic a-Si growth and subsequent doping by $POCl_3$ diffusion were carried out with N_2 as a carrier gas in LPCVD at 800 °C for 43 min. The doping level in the n-type poly-Si layer after diffusion was measured by electrochemical capacitance-voltage (ECV) as around 2 × 10^{20} cm^{-3}. Forming gas (10% H_2 in N_2) annealing was used to hydrogenate the poly-Si passivating contacts in precursor samples (400 °C, 30 min). Further details about the fabrication process can be found elsewhere.[39,40] For solar cell fabrication, the samples were single-side textured prior realizing rear and front ultrathin SiO_x/poly-Si CSPCs and received 4 min HF dip before depositing TCO in order to remove any eventual present surface oxide. In order to extract the contact resistivity of n-contact (n^+ poly-Si/TCO/metal) and p-contact (p^+ poly-Si/TCO/metal) from vertical dark current−voltage ($I-V$) measurements,[4,41] full-area 1 μm-thick Ag was evaporated on both sides of test structures in Figure 1b, in which n-type and p-type c-Si were utilized as substrates, respectively. The measurements were carried out on a Cascade33 Microtech setup in Else Kooi Lab at Delft University of Technology, with a four-point mode to eliminate the influence from the chuck and ensure accuracy of the extracted resistance R_{total} ($R_{total} = R_{base} + 2 \times R_{contact}$). Screen-printing Ag was used for solar cells metallization, and the curing condition was 170 °C for 30 min with a subsequent 350 °C for 5 min to restore the passivation in samples without TCO PDA treatments. During the fabrication of the contact stack and solar cells, we tracked the precursor passivation qualities (e.g., implied V_{oc}, i-V_{oc}) by using a Sinton WCT-120 with quasi-steady-state photoconductance (QSSPC) mode. SunsVoc measurements were performed as well for evaluating the electrical transport properties in our devices via a Sinton Suns-V_{OC}-150 Illumination-Voltage Tester. We characterized the $I-V$ performance and external quantum efficiency (EQE) of the solar cell by using an AAA class Wacom WXS-156S-L2 solar simulator and an in-house EQE setup.

3. RESULTS AND DISCUSSION

3.1. Opto-electrical Properties upon PDA Treatments.
Figure 2 illustrates data points of (N_e, μ_{Hall}) of the IFO:H films under different PDA treatments, i.e., Hall mobilities (μ_{Hall}) versus corresponding carrier densities (N_e) plot. Resistivity (ρ) lines are also provided according to the relation $\log(\mu_{Hall}) = -\log(N_e) + \log(1/\rho e)$.[42] Hall measurements show that all the films exhibit n-type conductivity. The mobilities (μ_{Hall}) are plotted versus the corresponding carrier densities (N_e), with
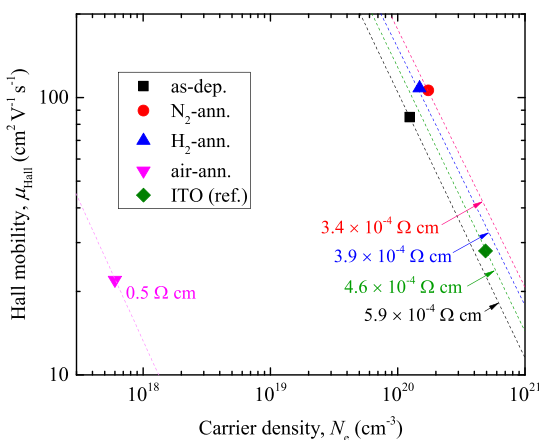

Figure 2. Hall mobilities (μ_{Hall}) versus corresponding carrier densities (N_e) of the IFO:H films under different PDA treatments. Lab-standard ITO layer is provided as a reference data point. Symbols are the measured (N_e, μ_{Hall}) pairs, while the dashed lines indicate resistivity values.

our lab-standard 80 nm-thick ITO data serving as a reference. Compared to the ITO reference, the as-dep. IFO:H film shows a bit higher resistivity, while the N_2-ann. and H_2-ann. layers show lower resistivity values. We note that the properties of the ITO layer also change with PDA treatments, but the topic is outside the scope of this article, thus will not be elaborated here. Among the IFO:H films, with respect to the as-dep. film, the reduced resistivity values in the N_2-ann. and H_2-ann. films result from improvements in both N_e and μ_{Hall}. In sharp contrast, the air-ann. sample shows instead an obvious deterioration in electrical properties, caused by largely reduced N_e and μ_{Hall}. The specific data of N_e, μ_{Hall} and sheet resistance (R_{sh}) of the IFO:H films under PDA are summarized in Table 2. The optimal material properties were obtained after PDA in hydrogen, with carrier density = 1.5 × 10^{20} cm^{-3}, electron mobility = 108 cm^2 V^{-1} s^{-1}, and resistivity = 3.9 × 10^{-4} Ω cm. In addition, the N_2-ann. sample shows comparable electrical properties as the H_2-ann. film, and detailed elucidation and supplement of these observations will be discussed in the following sections.

Furthermore, the optical properties of the IFO:H films were evaluated, as compared to the commonly used ITO. Figure 3a displays the measured wavelength-dependent transmittance/reflectance of the IFO:H films under different PDA treatments, with our lab-standard ITO layer as a reference. In the ultraviolet (UV) range, the transmittance edge of the ITO film and the air-ann. IFO:H sample basically showed a red shift with respect to the other IFO:H layers. These results imply optical band gap (E_g) differences of the IFO:H films, which are illustrated Figure 3b. The transmittance/reflectance differences around the 400−600 nm region among the IFO:H films might be caused by the different film thicknesses after PDA treatments (as shown in Table 2). Figure 3b shows the absorption coefficient curves extracted from ellipsometry (SE) fittings. As one can observe, contrasting with the ITO film, the IFO:H layers show a marked sharper transition at the absorption edge in the UV part and a visible lower absorption in the NIR region, which is in accordance with our previous report and underlines the great potential of the IFO:H film in allowing an augmented light in-coupling into the absorber material of PV devices.[12] Among the IFO:H films, with respect to the as-dep. film, the absorption edges of the N_2-ann. and H_2-ann. samples show blue shifts, while that of the air-ann. layer illustrates a red shift, indicating changes in E_g. The E_g for allowed direct electronic transition was extracted according to Tauc relation in Figure 3b, inset.[18,43] The E_g values of 3.85, 3.94, 3.87, 3.76, and 3.78 eV were obtained corresponding to as-dep., N_2-ann., H_2-ann., air-ann., and ITO reference samples, respectively. The results of IFO:H films are in accordance with the N_e changes in Hall measurements (as shown in Table 2), which can be explained by the Moss−Burstein effect in the degenerate semiconductors ($\Delta E_g \propto N_e^{2/3}$).[44] The wavelength-dependent complex refractive index of the films are reported in Supporting Information Figure S1, and repeated experimental opto-electrical parameters of IFO:H films under different PDA treatments can be found in Table S3.

To evaluate the conduction and valence band tail states change in the IFO:H film after various PDA treatments, we extracted the Urbach energy (E_U), which is presumed as the width of the tail of localized defect states in the band gap in low-crystalline, disordered, or amorphous materials.[43] We followed the equation $\ln \alpha = \ln \alpha_0 + (h\nu/E_U)$, where α is the absorption coefficient, α_0 is a pre-exponential constant, and $h\nu$

Table 2. Extracted Material Parameters of the IFO:H Films under Different PDA Treatments

samples	$^a d_b$ (nm)	$^a d_s$ (nm)	$^b N_e$ (10^{20} cm^{-3})	$^b \mu_{Hall}$ (cm^2 V^{-1} s^{-1})	$^c R_{sh}$ (Ω/sq)	$^d D_{crystallite}$ (nm)	$^e D_{grain}$ (nm)	^{e} RMS (nm)	$^a \mu_{opt}$ (cm^2 V^{-1} s^{-1})	$^a E_U$ (meV)
as-dep.	81.68	2.71	1.24	85	67	22.08	20.00	1.24	102	229
N$_2$-ann.	89.91	4.90	1.74	106	35	27.67	23.53	1.75	121	224
H$_2$-ann.	93.38	4.53	1.49	108	40	25.03	27.45	1.82	153	256
air-ann.	93.21	4.28	0.01	22	760	25.91	27.45	1.69	135	224

^{a}Determined from SE best fitting. ^{b}Measured from Hall setup. ^{c}Tested by the four-point probe technique. ^{d}Calculated from XRD data using Scherrer's formula. ^{e}Evaluated from AFM images in NOVA program.
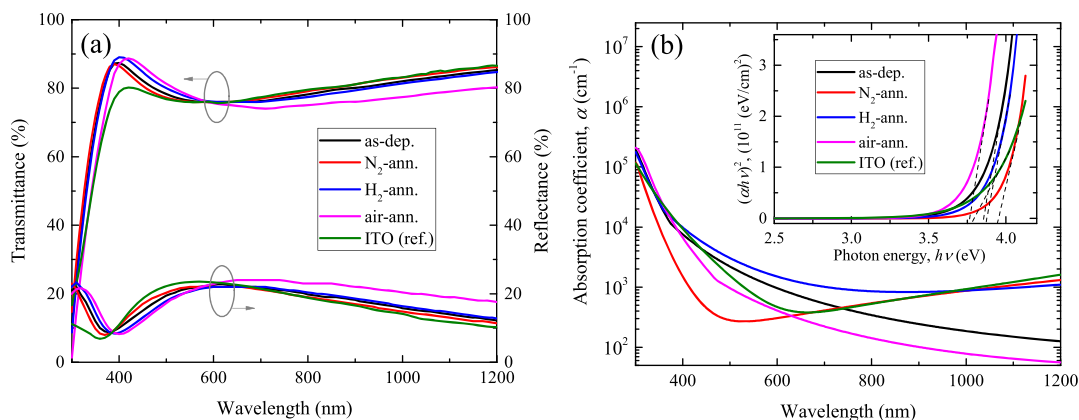

Figure 3. Optical properties of IFO:H films after various PDA treatments: (a) transmittance/reflectance spectra and (b) absorption coefficient curves from SE fitting; the inset is optical band gap plots.

is the incident photon.[43] The fitting results show E_U values of 229, 224, 256, 224, and 420 meV with as-dep., N$_2$-ann., H$_2$-ann., air-ann. IFO:H films, and reference ITO layer, respectively. The data for the as-deposited layers are at similar levels with our previous report.[12] Among the IFO:H films, with respect to the as-dep. sample, a relatively higher E_U value was observed in the H$_2$-ann. layer, implying increased band tail states and promoted atomic structural disorder.[24] This is plausibly caused by the hydrogen-induced defects such as interstitial H$_i$ dopants and V$_O$H shallow donor states (generated by hydrogen occupation on V$_O$ sites), but the position of the corresponding subgap states is still under debate.[24,45−47] By contrast, the N$_2$-ann. and air-ann. samples exhibit a bit lower E_U values with respect to the as-dep. sample, which might be attributed to the improved material quality during the annealing process.

3.2. Structure, Morphology, and Electron Scattering Mechanism of the IFO:H Films under Different PDA Treatments. *3.2.1. Structural/Morphological Changes under Different PDA Treatments.* Figure 4 shows the X-ray diffraction (XRD) patterns of the IFO:H thin films under various PDA treatments. All films display XRD peaks at $2\theta = 21.3°, 30.6°, 35.5°, 41.7°, 51.0°,$ and $60.6°$, corresponding to (211), (222), (400), (332), (440), and (622) planes of polycrystalline In$_2$O$_3$ with cubic bixbyite structure,[10,12,48,49] with the preferred (222) orientation. No crystalline orientation change was observed along with different PDA treatments. Furthermore, from Gaussian fitting, all the annealed layers exhibited smaller full-width at half-maximum (FWHM) value of X-ray peak of (222) than the as-deposited film, indicating larger crystallite sizes and smaller strains in the annealed films.[10,50] According to Scherrer's formula,[50] the mean crystallite size ($D_{crystallite}$) values from the (222) orientation are calculated to be 22.08, 27.67, 25.03, and 25.91 nm for as-dep., N$_2$-ann., H$_2$-ann., and air-ann. samples, respectively, as
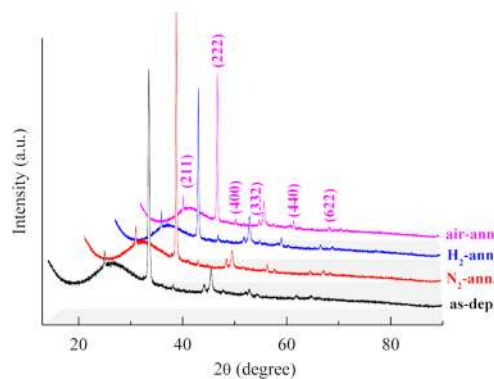

Figure 4. X-ray diffraction patterns of IFO:H films under different PDA treatments.

summarized in Table 2. The small peaks appearing at 43° probably originate from substrate contamination since they can hardly be assigned to indium oxide/fluoride materials. We further measured the as-deposited samples, which were done previously, and 1 month later, no such signals were detected anymore.

Figure 5a−d shows AFM images of the as-deposited, N$_2$-ann., H$_2$-ann., and air-ann. samples, respectively. In contrast to the as-dep. film, the annealed layers exhibit a rougher surface along with densely distributed granular structures. Enlarged grain sizes were observed in annealed samples compared to the as-dep. film, and we ascribe the observed agglomerated trend to the heating effect.[24] These spontaneously formed nanostructures have a size range of 20−30 nm. The grain size (D_{grain}) and the root-mean-square (RMS) roughness values of the samples are reported in Table 2.

3.2.2. Electron Scattering Mechanism in IFO:H Films under Different PDA Treatments. The carrier scattering
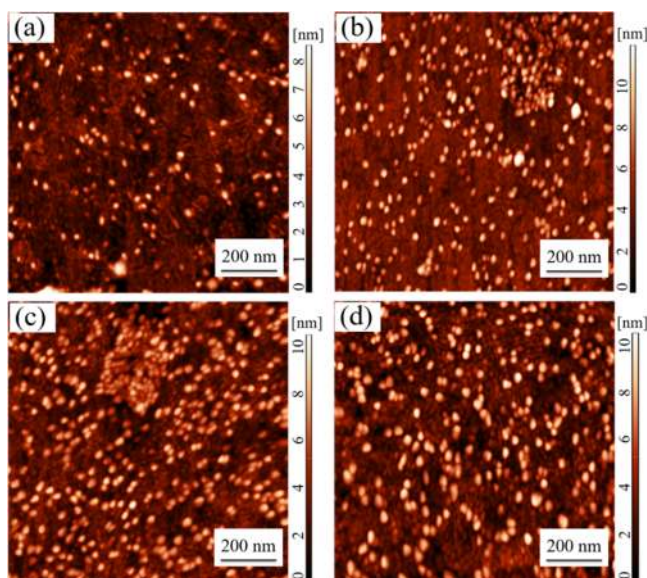
Figure 5. AFM micrographs of the (a) as-dep., (b) N_2-ann., (c) H_2-ann., and (d) air-ann. IFO:H films.

mechanism responsible for conductivity of the IFO:H thin films under different PDA treatments has been investigated. Note that, in terms of physical definition, $\mu = e\tau/m^*$, where μ is the carrier mobility, which directly correlates the conductivity parameter, τ and m^* are carrier relaxation time and electron effective mass, respectively. It has been theoretically[34] and experimentally[10] found that high-μ TCO films exhibit a similar m^* regardless of the material phase, and high μ is mainly achieved through a larger τ rather than a smaller m^*.[10] In polycrystalline films, the overall relaxation time is determined by scattering induced by grain boundaries (GBs), stacking faults, dislocations, charged centers such as ionized impurities, and phonons (lattice vibrations).[10]

First, to distinguish whether GBs play roles on carrier scattering in the IFO:H films under different PDA treatments, we made a comparison between μ_{Hall} and μ_{opt}, as summarized in Table 2. One can clearly see that $\mu_{Hall}/\mu_{opt} < 1$ occurs for all the samples, yielding information that grain boundary scattering contributes to the carrier scattering in both as-deposited and annealed IFO:H films (especially for the air-ann.

sample). To corroborate that, we further calculated the mean free path (MFP) of the charge carriers, which might represent an estimation of the upper limit for the distance between scattering centers.[33,51] Using the Fermi velocity $v_F = \hbar(3\pi^2 N_e)^{1/3}/m^*$, where $\hbar$ is the reduced Planck constant, and the scatter frequency $\omega_\tau = e/(m^*\mu_{opt})$, MFP = v_F/ω_τ values were found to be 10.38, 13.79, 15.92, and 2.33 nm for as-dep., N_2-ann., H_2-ann., and air-ann. samples, respectively. The MFP values are of the same order of magnitude as $D_{crystallite}$ and D_{grain}, implying that GBs could play a role in the conduction mechanisms of the IFO:H films. We note that for the air-ann. film, in which grain boundary scattering might be a dominating factor, the MFP value is less meaningful since grain boundaries do not really act as scattering centers in the intra-grain analysis.

Second, we carried out DB-PAS measurements to identify the open-volume defects and thus understand the doping mechanisms in the PDA-treated IFO:H layers. The positron is the antiparticle of the electron. The annihilation between positron and electron produces γ-quanta, which forms the detected signal. Since positrons are repelled by the positive charge of the atom cores, neutral and negatively charged vacancy defects usually act as positron traps. In particular, we used DB-PAS as an additional tool to examine whether V_O or V_OH vacancy defects are present as they are well known to act as donors in In_2O_3-based TCOs. While the positively charged V_O (or V_OH) alone does not trap positrons, V_O defects are detectable in DB-PAS when they are complexed with cation vacancies (namely, V_{In}-nVo complex).[52,53] Figure 6a shows the collected best-fit positron Doppler broadening W-parameters as a function of S-parameters of the IFO:H films using VEPFIT analysis, in which the as-dep. film denotes an $S-W$ reference point, and error bars were calculated as the average deviation of fitted values to measured data in the energy range of 1−2.5 keV where the targeted IFO:H film is probed (see Supporting Information, Figure S2 and Table S1). Specifically, the S-parameter provides sensitivity to the presence of open-volume defects, while the W-parameter is more dependent on the type of atoms surrounding the annihilation site.[38,53] From Figure 6a, the S-parameter of the N_2-ann. layer and of the as-dep. sample are basically the same within the error bar region, indicating similar defect concentrations in the films or possibly saturation trapping of positrons at the vacancy sites. This phenomenon does not explain the notable increase in carrier density N_e of
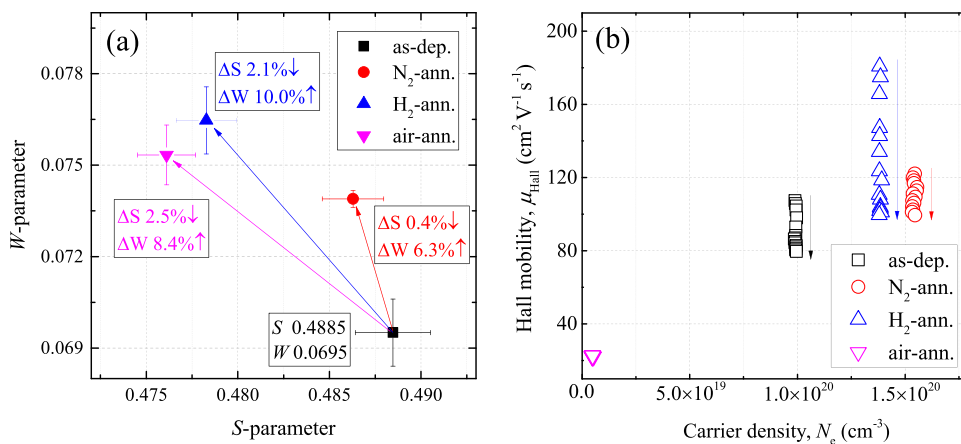

Figure 6. (a) $S-W$ parameters of the IFO:H films extracted from DB-PAS measurements. (b) Hall mobilities versus carrier densities in the IFO:H films in temperature-dependent Hall measurements; the arrows indicate the increasing direction of measurement temperature from 200 to 350 K.

~40% as shown in Table 2. The discrepancy plausibly results from the effective interstitial H_i dopants generated during the annealing procedure,[33] which contribute to the increased density in conduction band electrons but are invisible in DB-PAS measurements. In addition, the resulting S-parameter of the H_2-ann. sample is decreased by ~2.1% compared to the as-dep. Layer, implying a less vacancy-related defective film structure.[38] The reduced S may come from (i) a decrease in the size of V_O sites due to their occupation by H, making singly charged V_OH the major donor states in the film together with interstitial H_i,[10,33,45,54] which could explain the increased carrier density N_e in Table 2[23,45] and is in accordance with the increased subgap states from Urbach energy calculation in Section 3.1, or (ii) a reduction in the size of V_{In} sites due to their interaction with H impurities.[54] The above results outline the role of hydrogen-related donors as a dominant singly charged dopant in our IFO:H films, especially in N_2-ann. and H_2-ann. films. Furthermore, in the case of the air-ann. sample, the S-parameter is 2.5% lower than that of the as-dep. sample, indicating elimination of the V_{In}-nVo complex due to local oxidation,[53,55] which is also supported by a reported phenomenon[28] and the degraded electrical properties as shown in Hall measurements (Figure 2). On the other hand, all the W-parameters of the annealed samples show increased values with respect to the as-dep. layer, demonstrating a change in the local environment of vacancy defects, such as O occupying the V_O sites, or more effective fluorine impurities that order on neighboring V_{In} sites with improved crystallinity upon annealing (the fluorine impurities alone cannot act as positron annihilation sites). The experimental S- and W-parameter depth profiles and fit curves as a function of positron implantation energy for the IFO:H films under PDA are illustrated in Supporting Information, Figure S2, and the VEPFIT fitting parameters are provided in Table S1.

Third, we performed temperature-dependent Hall measurements to analyze the specific scattering mechanisms in the IFO:H films under different PDA treatments, as shown in Figure 6b. One can see that the N_e of the films does not show a temperature dependence as expected given the degenerate nature of the semiconductor.[56,57] In addition, the temperature dependence of the mobility of IFO:H greatly varies with different PDA treatments. Apart from the air-ann. sample, films exhibited a marked increase in μ_{Hall} with cooling direction with a negligible change in N_e, implying that phonon scattering plays notable role in the as-dep., N_2-ann., and H_2-ann films.[10]

Since mobility is inversely related to scattering, the separation into scattering processes is intuitively difficult. The interpretation becomes easier when using the inverse mobility.[33,51] According to Preissler et al.[29] and Macco et al.,[33] charged scattering centers from ionized impurities together with phonon scattering were found to be the dominant scattering mechanisms in both single-crystalline In_2O_3 and polycrystalline hydrogenated In_2O_3 films. Combined with the previous proven grain boundary scattering in our IFO:H films, we assume the temperature-dependent mobility can be expressed as follows from Matthiessen's rule:[33]

$$\frac{1}{\mu} = \frac{1}{\mu_{GB}} + \frac{1}{\mu_{cc}} + \frac{1}{\mu_0}\left(\frac{T}{T_0}\right)^p \qquad (1)$$

In this equation, μ_{GB} represents the mobility results from grain boundary scattering, and μ_{cc} is from charged scattering centers (such as V_O and V_OH). The last component in eq 1 is

the inverse phonon mobility (μ_{phonon}), in which μ_0 denotes the phonon mobility at a reference temperature T_0. The parameter p exponential fits temperature-dependent mobility data (see Supporting Information, Figure S3a). According to the literature, the fitted p values should be in the range of 2−4 if the temperature is below the Debye temperature (reported range for In_2O_3 is 420−811 K).[29,33] While our converged parameter p values were determined to be 1.35, 1.76, and 2.25 for as-dep., N_2-ann., and H_2-ann. samples, respectively. No converged p value was obtained for the air-ann. layer.

We note that, at the grain size range and carrier densities of interest (1×10^{20} to 2×10^{20} cm^{-3}), the grain boundary scattering can be either temperature-independent tunneling or temperature-dependent thermionic emission.[33,56,58,59] By assuming μ_{GB} as a temperature-independent component in eq 1, the latter case would not be displayed. That is why our obtained $1/\mu_{phonon}$ varies for different IFO:H films. On the other hand, the possible presence of thermionic emission can be roughly evaluated by the deviation on fitted p values from the abovementioned reasonable range of 2−4 according to eq 1. From the above results, only the p value of the H_2-ann. film is above 2 and is in accordance with the reported values for (un)intentionally hydrogen-doped In_2O_3 films.[33,35] This evidences that, in the H_2-ann. film, grain boundary scattering is in tunneling mode, while in as-dep. and N_2-ann. layers, thermionic emission and tunneling current may coexist at GBs. Additionally, we plotted $\mu_{Hall}\sqrt{T}$ versus inverse temperature for the air-ann. sample (see Supporting Information, Figure S3b), which showed exponential dependence that well matches the scattering mechanism described by the Schottky barrier model in thermionic emission.[57] It agrees with the report that, in the TCO film with rather low carrier densities (<10^{18} cm^{-3}), transport across grain boundaries would be mainly through thermionic emission.[56] Hence, we can conclude that thermionic grain boundary scattering is the dominant mechanism in the air-ann. layer.

Figure 7 plots a rough estimate on the inverse mobilities that accounts for carrier scattering from charged centers, phonons, and GBs based on eq 1. We decoupled components from the above mathematic fitting for the H_2-ann. film, and the fitted phonon mobility is ~150 cm^2 V^{-1} s^{-1}, which is in a similar
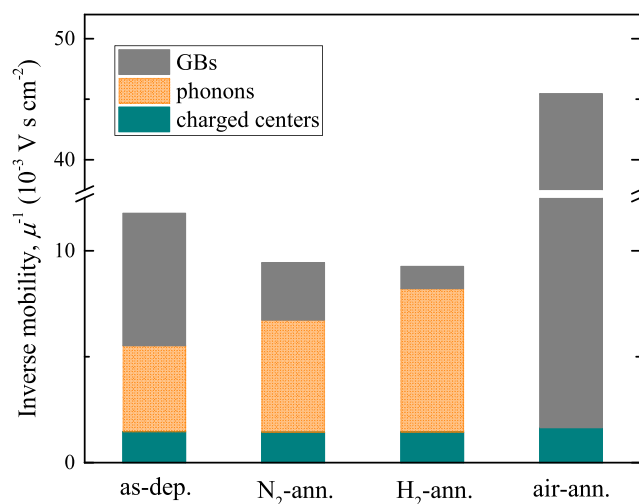

Figure 7. Inverse electron mobility components of IFO:H films under different PDA treatments.
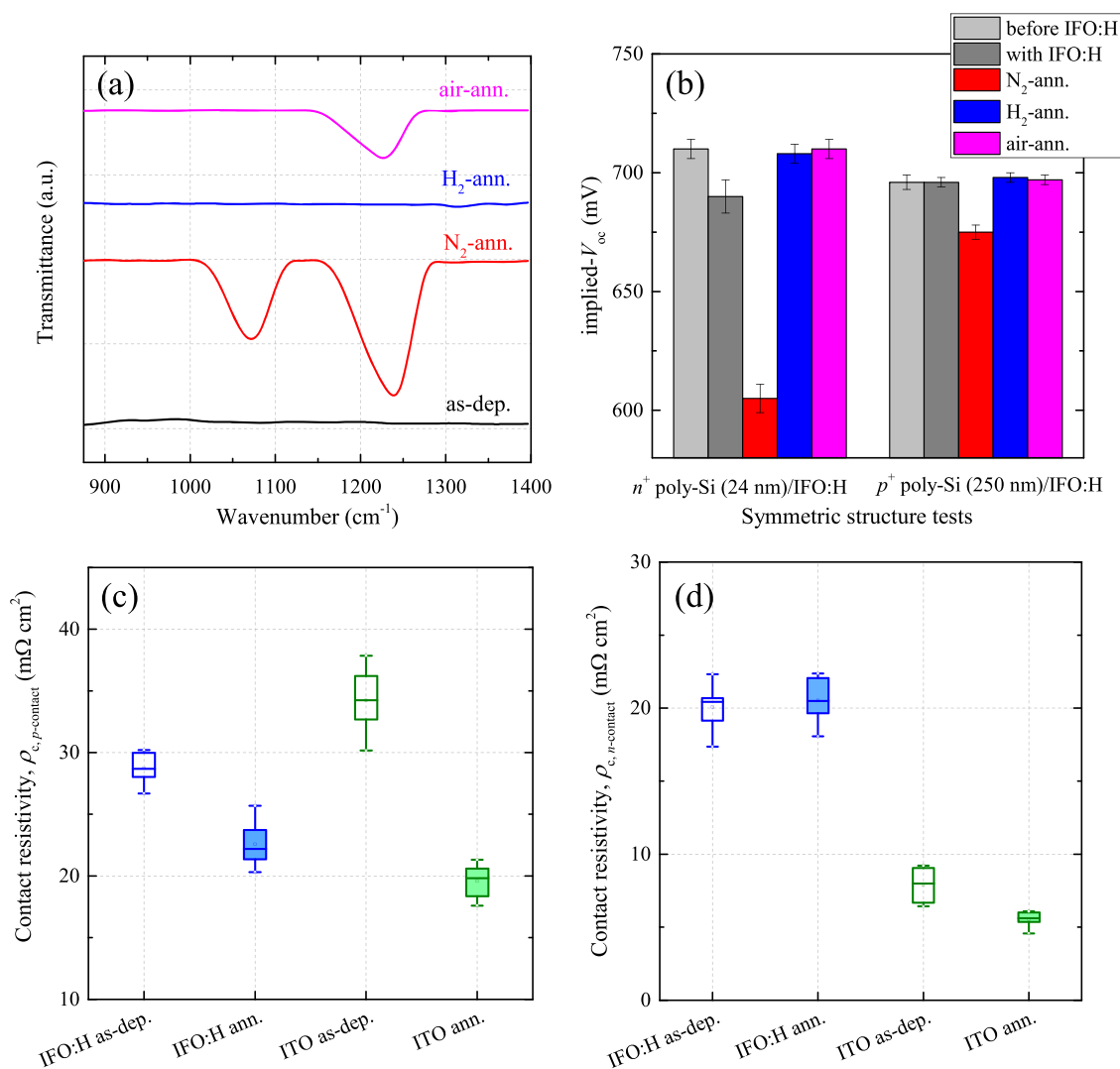
Figure 8. (a) Baseline-corrected FTIR spectra and (b) implied V_{oc} change of the poly-Si/IFO:H stack under different PDA treatments. Contact resistivities of (c) n-contact (n^+ poly-Si/TCO/metal) and (d) p-contact (p^+ poly-Si/TCO/metal) using IFO:H and ITO with and without H_2 annealing treatment, respectively. The results in (c) and (d) are collected based on six groups of experimental data.

level as predicted by Preissler et al.[29] In the cases of as-dep. and N_2-ann. films, thermionic emission at GBs results in converged p values deviating from the expected range for the phonon scattering component. The $1/\mu_{phonon}$ components in these films were assumed based on their p deviation from the H_2-ann. film (uncertainties therein). In the air-ann. film, thermionic emission at GBs dominates in the film, and phonon scattering is assumed to be negligible. In addition, for statistically homogeneously distributed scattering centers, the charged center limited mobility (μ_{cc}) were calculated following eq 2:[33,60]

$$\mu_{cc} = \frac{3(\varepsilon_r \varepsilon_0)^2 h^3}{Z^2 m^{*2} e^3} \frac{N_e}{N_i} \frac{1}{F_{cc}(\xi_0)} \qquad (2)$$

In this equation, h is Planck's constant, ε_0 and ε_r are the vacuum and relative permittivity (for In_2O_3, $\varepsilon_r = 8.9$), respectively, and $\xi_0 = (3\pi^2)^{1/3} \varepsilon_r \varepsilon_0 h^2 N_e^{1/3}/m^*e^2$. Z is the charge state of the ionized impurity, and N_i the concentration of ionized impurities (taken to be N_e/Z, i.e., full ionization is assumed). $F_{cc}(\xi_0)$ is the N_e-dependent screening function for charged center scattering given non-parabolicity of the band

structure.[60] Considering the DB-PAS analysis in Figure 6a, it is well possible that singly charged hydrogen-related dopants are prevalent in our IFO:H films (especially in N_2-ann. and H_2-ann. films). Hence, we assume singly charged donors dominate in the IFO:H films, i.e., $Z = 1$.

From Figure 7, we note that μ_{cc} almost remains at the same level for all the IFO:H films under different PDA treatments. In addition, in the as-dep. layer, μ_{GB}, μ_{phonon}, and μ_{cc} co-play in the film, which is in accordance with reported electron scattering mechanisms on polycrystalline hydrogenated indium oxide films.[61] In contrast to the as-dep. film, the N_2-ann. sample shows a decreased μ_{GB} contribution accompanied by an increased μ_{phonon} component, which is presumably caused by diminished GBs from crystallite growth and increased GB passivation by diffused hydrogen during the heating process.[23,45] Furthermore, in the H_2-ann. film, a pronounced μ_{phonon} component is observed (as expected), indicating a further improved hydrogen passivation on GBs with respect to the N_2-ann. sample. In addition, in the air-ann. sample, μ_{GB} absolutely dominates in the film.

3.3. Contact and Device Application. FTIR measurements were carried out to evaluate the interfacial oxide
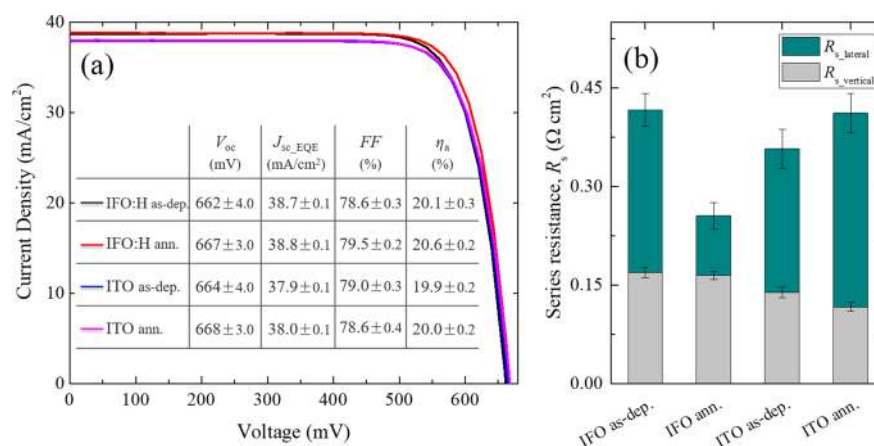
Figure 9. (a) Current−voltage characteristics of the best 3.92 cm^2 poly-Si solar cell devices using IFO:H and ITO with and without the H$_2$ annealing treatment, respectively. The values reported are the average based on three cells from the same batch, and more device results from different experimental batches can be found in Table S4. (b) Decomposition of series resistance ($R_{s, SunsVoc}$) that corresponds to (a).

formation on symmetric structures with n^+ poly-Si/IFO:H stack in Figure 1b; note that the FTIR results are collected on TCO coated poly-Si stacks. Figure 8a shows the baseline-corrected FTIR transmittance spectra of the IFO:H films under different PDA treatments by using the as-dep. sample as a reference baseline. In such a way, the noisy signals resulting from free carrier absorption of the TCOs in the infrared region were removed in the data reading so that the signal of our wanted n^+ poly-Si/TCO interfacial oxide formation was enlarged and became recognizable. The vibrations of the Si−O−Si network were observed at ∼1076 and/or ∼1236 cm^{-1} in N$_2$-ann. and air-ann. samples, corresponding to its transverse mode (TO) and longitudinal mode (LO),[62] respectively. According to Ishikawa et al.[63] and Liu et al.,[62] the LO mode becomes lower when the film thickness decreases and the TO may become so weak with decreased SiO$_x$ film thickness or changed chemical composition that TO can be hardly recognized on the spectrum. Thus, the decreased LO intensity and undetected TO mode in the air-ann. sample might indicate a thinner interfacial SiO$_x$ layer compared to the N$_2$-ann. sample. Moreover, both the LO and TO characteristics were not detectable in H$_2$-ann. samples, implying a basically unchanged interfacial composition with respect to the as-dep. sample baseline.

The interfacial oxide has been assumed as a legitimate explanation for forming a transport barrier on the TCO/doped silicon layer and should be avoided in device application.[4,6,7,41] Figure 8b displays the passivation test results on symmetric structures (Figure 1b). In contrast to the 24 nm-thick n-poly stack, the 250 nm-thick p-poly stack shows a higher stability against sputter-induced degradation and PDA treatments. The thickness-dependent characteristic can be attributed to the role of the poly-Si film as shielding the critical c-Si/SiO$_x$/poly-Si interface from emerging harmful species.[4] The poly-Si thickness of 24 nm is in the reported range of 10−28 nm, in which the lifetime samples are dramatically sensitive during the subsequent process.[4] Hence, one can see a clear implied V_{oc} (i-V_{oc}) drop of ∼20 mV on the thin n-poly stack samples after sputtering, which goes further down after PDA in N$_2$ ambiance while almost get fully restored after PDA in H$_2$ and air atmosphere. Hydrogen has been widely accepted as a crucial factor for ensuring good passivation quality in the poly-Si passivating contacts;[64,65] thus, we attribute the passivation

recovery to a sufficient hydrogen supplement to the n^+ poly-Si/SiO$_x$/c-Si interfaces for the H$_2$-ann. sample. As for the air-ann. sample, with the existence of moisture (H$_2$O), the exchange of hydrogen at the n^+ poly-Si/SiO$_x$/c-Si interfaces do not harm the passivation qualities since water vapor has been reported to effectively hydrogenate the poly-Si passivating contacts.[66] While for the N$_2$-ann. contacts, the passivation degradation is plausibly caused by a dehydrogenation of the passivating contacts; in other words, hydrogen effuses from the n^+ poly-Si/SiO$_x$/c-Si interfaces. Additionally, we extracted one group of contact resistivity values (ρ_c) of n-contact (n^+ poly-Si/TCO/metal) regarding different PDA treatments, which showed the results of 21.68, 598.76, 22.05, and 265.05 mΩ cm^2, for as-dep., N$_2$-ann, H$_2$-ann, and air-ann. samples, respectively. We consider these values basically in accordance with Figure 8a, namely, the thicker interfacial oxide layer results in higher ρ_c values. From all the above results regarding both TCO opto-electrical properties and device application, we can conclude that the H$_2$ annealing treatment provides a promising contact engineering approach in the high thermal-budget poly-Si solar cell design.

To verify that, we extracted ρ_c values of n-contact (n^+ poly-Si/TCO/metal) and p-contact (p^+ poly-Si/TCO/metal) with and without the hydrogen annealing procedure, as shown in Figure 8c,d. Results on the lab-standard ITO layer were also provided for the audience's reference. As it can be seen, low ρ_c values below 40 mΩ cm^2 were observed for the contacts with as-deposited TCOs, which decreased further to around (or below) 20 mΩ cm^2 after the hydrogen annealing treatment. For the p-contact, which will be used on the rear side of the device (Figure 1c), all the $\rho_{c, p\text{-contact}}$ values after annealing were observed well below 30 mΩ cm^2, which will add negligible transport and FF losses when this stack is applied as a full-area contact.[7] As for the n-contact, to make a comparison, our $\rho_{c, n\text{-contact}}$ values with as-deposited ITO are comparable with the reported data with the 35 nm-thick n^+ poly-Si layer.[41] However, carrier transport at the poly-Si/TCO contact have been widely reported to degrade severely for temperatures above 350 °C (even >10^4 mΩ cm^2).[6,7,41] According to Tutsch et al., exposure at 380 °C in air significantly increased the ρ_c of n-contact from 50 to above 700 mΩ cm^2,[4] and Wietler et al. reported the unfavorable ρ_c of ∼800 mΩ cm^2 on a metal/ZnO:Al/poly-Si stack after air annealing at 400 °C.[6] To our

knowledge, the $\rho_{c,\,n\text{-contact}}$ values are among the lowest values reported so far for the poly-Si/TCO/metal stack with a <30 nm thin polysilicon layer, especially after thermal annealing at a high temperature.

It is widely accepted that parasitic growth of the interfacial oxide in thermal annealing might be the reason for the reported high contact resistivity at poly-Si/TCO after the annealing procedure.[7] According to the simulated results from Messmer et al.,[7] there is a critical parasitic oxide thickness of about 1.4 nm; below such value, the electron tunneling through the oxide is expected to be efficient to yield a low contact resistivity. Above this threshold, the contact resistivity grows exponentially with a linear increase in interfacial oxide thickness. Under this hypothesis, the un-increased contact resistivity values after our hydrogen annealing treatment at 400 °C probably result from the depression on the mentioned parasitic growth of interfacial oxide, which is also evidenced by our FTIR measurement results (Figure 8a). However, electric states at the interface between TCO and silicon can be very complicated (interface region can be even up to 50 nm[67]); thus, detailed investigation remains to be carried out. Additionally, we noticed that, for n-contact, ITO showed a lower ρ_c and a more preferable contact compared to IFO:H, which is inconsistent with our previous results.[12] This discrepancy might be explained by the high doping levels of the doped silicon layer and ITO,[7,68] which facilitate electron tunnelings at the n^+ poly-Si/TCO interface; thus, the work function matching becomes not as dominant as the case in ref 12.

Considering that H_2 annealing at 400 °C ensures good contact properties for both n-contact and p-contact, we tested the performance on completed devices. Figure 9a displays the poly-Si solar cell parameters in devices using IFO:H and ITO with and without the H_2 annealing treatment, respectively. Our devices experienced a general severe passivation loss accompanying the screen-printing procedure, which brought a big drop from i-V_{oc} (~710 mV) on cell precursors to V_{oc} values (~665 mV) in devices. This results from the damage of the metallization procedure on the (thin) poly-Si layer.[39,69] Corresponding solutions are under investigation. Apart from the general V_{oc} limitation on our devices, one can see that all the poly-Si solar cells showed similar V_{oc} values, which is in accordance with the results as shown in Figure 8b. In addition, the FF was clearly improved by 0.9%$_{abs.}$ (from 78.6 to 79.5%) with the H_2 annealing treatment for IFO:H-based cells. To elaborate this, we performed SunsVoc measurements and calculated the series resistance ($R_{s,\,SunsVoc}$) values of the devices according to eq 3:[70]

$$R_{s,SunsVoc} = (PFF - FF)\frac{V_{oc}J_{sc}}{J_{mpp}^2} \qquad (3)$$

In eq 3, PFF and J_{mpp} represent the pseudo fill factor and current density at maximum power point condition in SunsVoc measurements, respectively.

The specific vertical resistance ($R_{s,\,vertical}$) and lateral resistance ($R_{s,\,lateral}$) in our devices were then derived according to eqs 4 and 5, respectively. Figure 9b illustrates the calculative $R_{s,\,vertical}$ and $R_{s,\,lateral}$ results corresponding to the devices in Figure 9a:

$$R_{s,vertical} = \left(\frac{\rho_{c,n-contact}}{A_{front}} + \frac{\rho_{c,p-contact}}{A_{rear}} + \rho_{wafer}\frac{t_{wafer}}{A_{cell}}\right)\cdot A_{cell} \qquad (4)$$

In eq 4, $\rho_{c,\,n\text{-contact}}$ and $\rho_{c,\,p\text{-contact}}$ are corresponding average results from Figure 8c,d, respectively. A_{front}, A_{rear}, and A_{cell} denote the front metal coverage area, rear metal coverage area, and specific cell area, respectively. In our case, $A_{rear} = A_{cell}$. ρ_{wafer} is the wafer resistivity (we took 3 Ω cm in the calculation), and t_{wafer} is the wafer thickness (we took 270 μm as the single-side textured wafer). The vertical resistance values from our n^+ poly-Si, p^+ poly-Si, and TCO were negligible in the calculation:

$$R_{s,lateral} = R_{s,SunsVoc} - R_{s,vertical} \qquad (5)$$

From Figure 9b, the FF increase in the IFO:H ann. sample as compared to the IFO:H as-dep. sample is mainly caused by a decreased $R_{s,\,lateral}$ value, which can be reasonably attributed to the improved lateral conductivity of the IFO:H film (as shown in Table 2). Meanwhile, the $R_{s,\,vertical}$ almost remains unchanged in both kinds of samples, indicating that the small contact resistivity change as shown in Figure 8c,d did not bring an observable FF increase on IFO:H ann. devices with respect to IFO:H as-dep. cells. As for the comparative results on ITO-based devices, an average FF drop of 0.4%$_{abs.}$ after the hydrogen annealing treatment was observed. As it can be interpreted in Figure 9b, the FF drop is mainly caused by a decreased lateral conductivity of the ITO film, which plausibly results from stability issues of the ITO layer during the thermal treatments such as the firing steps in the screen-printing process. Such stability issues of ITO are beyond the scope of this article and will not be discussed here.

Furthermore, the as-deposited ITO-based devices showed a higher average FF of 79.0% than the 78.6% of the as-deposited IFO:H cell, which are consistent with our previous data (Figures 2a and 8c,d). Meanwhile, in the optical perspective, for specific TCO utilizations, slight J_{sc_EQE} improvements were observed after the H_2 annealing treatment, which might be interpreted by the compensation between E_g, n and FCA with the PDA treatment (Figure 3 and Figure S1). However, all the IFO:H cells outperformed ITO cells due to the optical advantage of the high-μ_e IFO:H film.[10,12] Subsequent improvements are under investigation regarding further reducing poly-Si layer thickness on the illuminated side, increasing internal reflection, etc.

Conclusively, the PDA with H_2 annealing at 400 °C was successfully utilized in high thermal-budget poly-Si solar cells, and no obvious FF loss was observed. An absolute 0.5% gain in active-area power conversion efficiency (η_a) was observed on IFO:H solar cells after the PDA treatment in H_2 ambience, mainly due to the FF improvement (0.9%$_{abs.}$). Additionally, with respect to the widely used ITO, the PDA-treated IFO:H layer maintains its optical advantages in terms of higher E_g (T) and lower FCA while improves its lateral conductivity. This makes it a competitive transparent electrode for photovoltaic devices especially for high thermal-budget solar cells.

4. CONCLUSIONS

In summary, we studied the opto-electrical properties of the hydrogenated fluorine-doped indium oxide (IFO:H) by means of post-deposition annealing (PDA) treatments at 400 °C in N_2, H_2, and air ambience. Through detailed analyses of the crystal structure, surface morphology, optical properties, and

temperature-dependent electrical properties, the inherent electron scattering and doping mechanisms of the IFO:H films were revealed and compared. Hydrogen annealing proved to provide an effective strategy that can simultaneously alter the opto-electrical properties of the TCO film and maintain a favorable carrier transport at the poly-Si/TCO contact. We highlight that the low contact resistivity of around (or below) 20 mΩ cm^2 was achieved on both n- and p-contacts with poly-Si/TCO stack after hydrogen annealing, which to our knowledge is among the lowest values especially on thermally annealed contacts at 400 °C. Beyond this, we successfully implemented the hydrogen-annealed IFO:H films on FBC poly-Si solar cells. A 0.9%$_{abs}$ improvement in fill factor was observed, which leads to an absolute 0.5% gain in active-area power conversion efficiency on poly-Si solar cells with IFO:H. We believe our findings will provide important insight for future material/contact engineering in various photovoltaic devices endowed with TCOs such as IFO:H.

■ ASSOCIATED CONTENT

Ⓢ Supporting Information

The Supporting Information is available free of charge at https://pubs.acs.org/doi/10.1021/acsaem.0c01206.

Complex refractive index from SE fitting, S- and W-parameters and corresponding fitting parameters in DB-PAS analysis, temperature-dependent Hall mobilities, and repeated results from different batches (PDF)

■ AUTHOR INFORMATION

Corresponding Authors

Can Han − *Photovoltaic Materials and Devices group, Delft University of Technology, Delft 2628 CD, The Netherlands; Shenzhen Institute of Wide-bandgap Semiconductors, Shenzhen 518055, China;* ⓞ orcid.org/0000-0002-3213-6856; Email: c.han-1@tudelft.nl

Olindo Isabella − *Photovoltaic Materials and Devices group, Delft University of Technology, Delft 2628 CD, The Netherlands;* Email: o.isabella@tudelft.nl

Authors

Guangtao Yang − *Photovoltaic Materials and Devices group, Delft University of Technology, Delft 2628 CD, The Netherlands*

Ana Montes − *Photovoltaic Materials and Devices group, Delft University of Technology, Delft 2628 CD, The Netherlands; Faculty of Sciences of University of Lisbon, Lisbon 1749-06, Portugal*

Paul Procel − *Photovoltaic Materials and Devices group, Delft University of Technology, Delft 2628 CD, The Netherlands*

Luana Mazzarella − *Photovoltaic Materials and Devices group, Delft University of Technology, Delft 2628 CD, The Netherlands*

Yifeng Zhao − *Photovoltaic Materials and Devices group, Delft University of Technology, Delft 2628 CD, The Netherlands*

Stephan Eijt − *Department of Radiation Science and Technology, Faculty of Applied Sciences, Delft University of Technology, Delft 2629 JB, The Netherlands*

Henk Schut − *Department of Radiation Science and Technology, Faculty of Applied Sciences, Delft University of Technology, Delft 2629 JB, The Netherlands*

Xiaodan Zhang − *Institute of Photoelectronic Thin Film Devices and Technology of Nankai University, Tianjin 300350, China;* ⓞ orcid.org/0000-0002-0522-5052

Miro Zeman − *Photovoltaic Materials and Devices group, Delft University of Technology, Delft 2628 CD, The Netherlands*

Complete contact information is available at:
https://pubs.acs.org/10.1021/acsaem.0c01206

Author Contributions

The manuscript was written through contributions of all authors. All authors have given approval to the final version of the manuscript.

Notes

The authors declare no competing financial interest.

■ ACKNOWLEDGMENTS

■ REFERENCES

(1) Hermle, M.; Feldmann, F.; Bivour, M.; Goldschmidt, J. C.; Glunz, S. W. Passivating contacts and tandem concepts: Approaches for the highest silicon-based solar cell efficiencies. *Appl. Phys. Rev.* **2020**, 7, No. 021305.

(2) Liu, W.; Yang, X.; Kang, J.; Li, S.; Xu, L.; Zhang, S.; Xu, H.; Peng, J.; Xie, F.; Fu, J.-H.; Wang, K.; Liu, J.; Alzahrani, A.; De Wolf, S. Polysilicon Passivating Contacts for Silicon Solar Cells: Interface Passivation and Carrier Transport Mechanism. *ACS Appl. Energy Mater.* **2019**, 2, 4609−4617.

(3) Allen, T. G.; Bullock, J.; Yang, X.; Javey, A.; De Wolf, S. Passivating contacts for crystalline silicon solar cells. *Nat. Energy* **2019**, 4, 914−928.

(4) Tutsch, L.; Feldmann, F.; Polzin, J.; Luderer, C.; Bivour, M.; Moldovan, A.; Rentsch, J.; Hermle, M. Implementing transparent conducting oxides by DC sputtering on ultrathin SiO$_x$ / poly-Si passivating contacts. *Sol. Energy Mater. Sol. Cells* **2019**, 200, 109960.

(5) Limodio, G.; Yang, G.; De Groot, Y.; Procel, P.; Mazzarella, L.; Weber, A. W.; Isabella, O.; Zeman, M. Implantation-based passivating contacts for crystalline silicon front/rear contacted solar cells. *Progr. Photovolt.: Res. Appl.* **2020**, 28, 403−416.

(6) Wietler, T. F.; Min, B.; Reiter, S.; Larionova, Y.; Reineke-Koch, R.; Heinemeyer, F.; Brendel, R.; Feldhoff, A.; Krügener, J.; Tetzlaff, D.; Peibst, R. High Temperature Annealing of ZnO:Al on Passivating POLO Junctions: Impact on Transparency, Conductivity, Junction Passivation, and Interface Stability. *IEEE J. Photovoltaics* **2019**, 9, 89−96.

(7) Messmer, C.; Bivour, M.; Luderer, C.; Tutsch, L.; Schön, J.; Hermle, M. Influence of Interfacial Oxides at TCO/Doped Si Thin Film Contacts on the Charge Carrier Transport of Passivating Contacts. *IEEE J. Photovoltaics* **2019**, 10, 1−350.

(8) Yoon, W.; Scheiman, D.; Ok, Y.-W.; Song, Z.; Chen, C.; Jernigan, G.; Rohatgi, A.; Yan, Y.; Jenkins, P. Sputtered indium tin oxide as a recombination layer formed on the tunnel oxide/poly-Si passivating contact enabling the potential of efficient monolithic perovskite/Si tandem solar cells. *Sol. Energy Mater. Sol. Cells* **2020**, 210, 110482.

(9) Wimmer, M.; Bär, M.; Gerlach, D.; Wilks, R. G.; Scherf, S.; Lupulescu, C.; Ruske, F.; Félix, R.; Hüpkes, J.; Gavrila, G.; Gorgoi, M.; Lips, K.; Eberhardt, W.; Rech, B. Hard x-ray photoelectron spectroscopy study of the buried Si/ZnO thin-film solar cell interface:

Direct evidence for the formation of Si−O at the expense of Zn-O bonds. *Appl. Phys. Lett.* **2011**, *99*, 152104.

(10) Koida, T.; Ueno, Y.; Shibata, H. In_2O_3-Based Transparent Conducting Oxide Films with High Electron Mobility Fabricated at Low Process Temperatures. *Phys. Status Solidi A* **2018**, *215*, 1700506.

(11) Morales-Masis, M.; Rucavado, E.; Monnard, R.; Barraud, L.; Holovský, J.; Despeisse, M.; Boccard, M.; Ballif, C. Highly Conductive and Broadband Transparent Zr-Doped In_2O_3 as Front Electrode for Solar Cells. *IEEE J. Photovoltaics* **2018**, *8*, 1202−1207.

(12) Han, C.; Mazzarella, L.; Zhao, Y.; Yang, G.; Procel, P.; Tijssen, M.; Montes, A.; Spitaleri, L.; Gulino, A.; Zhang, X.; Isabella, O.; Zeman, M. High-Mobility Hydrogenated Fluorine-Doped Indium Oxide Film for Passivating Contacts c-Si Solar Cells. *ACS Appl. Mater. Interfaces* **2019**, *11*, 45586−45595.

(13) Swallow, J. E. N.; Williamson, B. A. D.; Sathasivam, S.; Birkett, M.; Featherstone, T. J.; Murgatroyd, P. A. E.; Edwards, H. J.; Lebens-Higgins, Z. W.; Duncan, D. A.; Farnworth, M.; Warren, P.; Peng, N.; Lee, T.-L.; Piper, L. F. J.; Regoutz, A.; Carmalt, C. J.; Parkin, I. P.; Dhanak, V. R.; Scanlon, D. O.; Veal, T. D. Resonant doping for high mobility transparent conductors: the case of Mo-doped In_2O_3. *Mater. Horiz.* **2020**, *7*, 236−243.

(14) Aydin, E.; De Bastiani, M.; Yang, X.; Sajjad, M.; Aljamaan, F.; Smirnov, Y.; Hedhili, M. N.; Liu, W.; Allen, T. G.; Xu, L.; Van Kerschaver, E.; Morales-Masis, M.; Schwingenschlögl, U.; De Wolf, S. Zr-Doped Indium Oxide (IZRO) Transparent Electrodes for Perovskite-Based Tandem Solar Cells. *Adv. Funct. Mater.* **2019**, *29*, 1901741.

(15) Kobayashi, E.; Watabe, Y.; Yamamoto, T.; Yamada, Y. Cerium oxide and hydrogen co-doped indium oxide films for high-efficiency silicon heterojunction solar cells. *Sol. Energy Mater. Sol. Cells* **2016**, *149*, 75−80.

(16) Runnerstrom, E. L.; Bergerud, A.; Agrawal, A.; Johns, R. W.; Dahlman, C. J.; Singh, A.; Selbach, S. M.; Milliron, D. J. Defect engineering in plasmonic metal oxide nanocrystals. *Nano Lett.* **2016**, *16*, 3390−3398.

(17) Kim, Y. H.; Kim, J. S.; Kim, W. M.; Seong, T.-Y.; Lee, J.; Müller-Meskamp, L.; Leo, K. Realizing the Potential of ZnO with Alternative Non-Metallic Co-Dopants as Electrode Materials for Small Molecule Optoelectronic Devices. *Adv. Funct. Mater.* **2013**, *23*, 3645−3652.

(18) Singh, S. P.; Raza, A.; Sharma, A. K.; Agnihotri, O. P.; Tewari, L. M. Characterization of fluorine-doped In_2O_3 films synthesized by spray pyrolysis. *Thin Solid Films* **1983**, *105*, 131−138.

(19) Barraud, L.; Holman, Z. C.; Badel, N.; Reiss, P.; Descoeudres, A.; Battaglia, C.; De Wolf, S.; Ballif, C. Hydrogen-doped indium oxide/indium tin oxide bilayers for high-efficiency silicon hetero-junction solar cells. *Sol. Energy Mater. Sol. Cells* **2013**, *115*, 151−156.

(20) Li, S.; Shi, Z.; Tang, Z.; Li, X. Study on the hydrogen doped indium oxide for silicon heterojunction solar cell application. *J. Alloys Compd.* **2017**, *705*, 198−204.

(21) Reunchan, P.; Zhou, X.; Limpijumnong, S.; Janotti, A.; Van de Walle, C. G. Vacancy defects in indium oxide: An ab-initio study. *Curr. Appl. Phys.*. **2011**, *11*, S296−S300.

(22) De Wit, J. H. W. The high temperature behavior of In_2O_3. *J. Solid State Chem.* **1975**, *13*, 192−200.

(23) Koida, T.; Kondo, M.; Tsutsumi, K.; Sakaguchi, A.; Suzuki, M.; Fujiwara, H. Hydrogen-doped In_2O_3 transparent conducting oxide films prepared by solid-phase crystallization method. *J. Appl. Phys.* **2010**, *107*, No. 033514.

(24) Arooj, S.; Xu, T.; Hou, X.; Wang, Y.; Tong, J.; Chu, R.; Liu, B. Green emission of indium oxide via hydrogen treatment. *RSC Adv.* **2018**, *8*, 11828−11833.

(25) Limpijumnong, S.; Reunchan, P.; Janotti, A.; Van de Walle, C. G. Hydrogen doping in indium oxide: An ab initio study. *Phys. Rev. B* **2009**, *80*, 193202.

(26) Cartier, E.; Stathis, J. H.; Buchanan, D. A. Passivation and depassivation of silicon dangling bonds at the Si/SiO_2 interface by atomic hydrogen. *Appl. Phys. Lett.* **1993**, *63*, 1510−1512.

(27) Tutsch, L.; Feldmann, F.; Macco, B.; Bivour, M.; Kessels, E.; Hermle, M. Improved Passivation of n-Type Poly-Si Based Passivating Contacts by the Application of Hydrogen-Rich Transparent Conductive Oxides. *IEEE J. Photovoltaics* **2020**, *10*, 986−991.

(28) Khlayboonme, S. T.; Thowladda, W. Comparative Study of Non-Annealing and Annealing on Properties of ITO Deposited by RF Magnetron Sputtering. *Key Eng. Mater.* **2015**, *659*, 615−619.

(29) Preissler, N.; Bierwagen, O.; Ramu, A. T.; Speck, J. S. Electrical transport, electrothermal transport, and effective electron mass in single-crystalline In_2O_3 films. *Phys. Rev. B* **2013**, *88*, No. 085305.

(30) Synowicki, R. A. Suppression of backside reflections from transparent substrates. *Phys. Status Solidi C* **2008**, *5*, 1085−1088.

(31) Ferlauto, A. S.; Ferreira, G. M.; Pearce, J. M.; Wronski, C. R.; Collins, R. W.; Deng, X.; Ganguly, G. Analytical model for the optical functions of amorphous semiconductors from the near-infrared to ultraviolet: Applications in thin film photovoltaics. *J. Appl. Phys.* **2002**, *92*, 2424−2436.

(32) Fujiwara, H.; Kondo, M. Effects of carrier concentration on the dielectric function of ZnO:Ga andIn_2O_3:Snstudied by spectroscopic ellipsometry: Analysis of free-carrier and band-edge absorption. *Phys. Rev. B* **2005**, *71*, No. 075109.

(33) Macco, B.; Knoops, H. C. M.; Kessels, W. M. M. Electron Scattering and Doping Mechanisms in Solid-Phase-Crystallized In_2O_3:H Prepared by Atomic Layer Deposition. *ACS Appl. Mater. Interfaces* **2015**, *7*, 16723−16729.

(34) Medvedeva, J. E. Combining Optical Transparency with Electrical Conductivity: Challenges and Prospects. *Transparent Electron.* **2010**, 1−29.

(35) Bierwagen, O.; Speck, J. S. High electron mobility In_2O_3 (001) and (111) thin films with nondegenerate electron concentration. *Appl. Phys. Lett.* **2010**, *97*, No. 072103.

(36) Avaritsiotis, J. N.; Howson, R. P. Composition and conductivity of fluorine-doped conducting indium oxide films prepared by reactive ion plating. *Thin Solid Films* **1981**, *77*, 351−357.

(37) Ritzau, K.-U.; Behrendt, T.; Palaferri, D.; Bivour, M.; Hermle, M. Hydrogen doping of Indium Tin Oxide due to thermal treatment of hetero-junction solar cells. *Thin Solid Films* **2016**, *599*, 161−165.

(38) Montes, A.; Eijt, S. W. H.; Tian, Y.; Gram, R.; Schut, H.; Suemasu, T.; Usami, N.; Zeman, M.; Serra, J.; Isabella, O. Point defects in $BaSi_2$ thin films for photovoltaic applications studied by positron annihilation spectroscopy. *J. Appl. Phys.* **2020**, *127*, No. 085304.

(39) Yang, G.; Ingenito, A.; Van Hameren, N.; Isabella, O.; Zeman, M. Design and application of ion-implanted polySi passivating contacts for interdigitated back contact c-Si solar cells. *Appl. Phys. Lett.* **2016**, *108*, No. 033903.

(40) Yang, G.; Ingenito, A.; Isabella, O.; Zeman, M. IBC c-Si solar cells based on ion-implanted poly-silicon passivating contacts. *Sol. Energy Mater. Sol. Cells* **2016**, *158*, 84−90.

(41) Tutsch, L.; Feldmann, F.; Bivour, M.; Wolke, W.; Hermle, M.; Rentsch, J. Integrating transparent conductive oxides to improve the infrared response of silicon solar cells with passivating rear contacts. In *AIP Conference Proceedings*; AIP Publishing LLC, 2018; Vol. *1999*, p 040023.

(42) Kasap, S.; Capper, P. *Handbook of electronic and photonic materials*; Springer, 2017, 1391−1395.

(43) Hassanien, A. S.; Akl, A. A. Effect of Se addition on optical and electrical properties of chalcogenide CdSSe thin films. *Superlattices Microstruct.* **2016**, *89*, 153−169.

(44) Köstlin, H.; Jost, R.; Lems, W. Optical and electrical properties of doped In_2O_3 films. *Phys. Status Solidi A* **1975**, *29*, 87−93.

(45) Nakashima, M.; Oota, M.; Ishihara, N.; Nonaka, Y.; Hirohashi, T.; Takahashi, M.; Yamazaki, S.; Obonai, T.; Hosaka, Y.; Koezuka, J. Origin of major donor states in In−Ga−Zn oxide. *J. Appl. Phys.* **2014**, *116*, 213703.

(46) Claflin, B.; Fritzsche, H. The role of oxygen diffusion in photoinduced changes of the electronic and optical properties in amorphous indium oxide. *J. Electron. Mater.* **1996**, *25*, 1772−1777.

(47) Morales-Masis, M.; de Nicolas, S. M.; Holovsky, J.; de Wolf, S.; Ballif, C. Low-Temperature High-Mobility Amorphous IZO for Silicon Heterojunction Solar Cells. *IEEE J. Photovoltaics* **2015**, *5*, 1340−1347.

(48) Kobayashi, H.; Ishida, T.; Nakamura, K.; Nakato, Y.; Tsubomura, H. Properties of indium tin oxide films prepared by the electron beam evaporation method in relation to characteristics of indium tin oxide/silicon oxide/silicon junction solar cells. *J. Appl. Phys.* **1992**, *72*, 5288−5293.

(49) Wu, W.-F.; Chiou, B.-S.; Hsieh, S.-T. Effect of sputtering power on the structural and optical properties of RF magnetron sputtered ITO films. *Semicond. Sci. Technol.* **1994**, *9*, 1242.

(50) Parsianpour, E.; Raoufi, D.; Roostaei, M.; Sohrabi, B.; Samavat, F. Characterization and Structural Property of Indium Tin Oxide Thin Films. *Adv. Mater. Phys. Chem.* **2017**, *07*, 42−57.

(51) Knoops, H. C. M.; van de Loo, B. W. H.; Smit, S.; Ponomarev, M. V.; Weber, J.-W.; Sharma, K.; Kessels, W. M. M.; Creatore, M. Optical modeling of plasma-deposited ZnO films: Electron scattering at different length scales. *J. Vac. Sci. Technol., A* **2015**, *33*, No. 021509.

(52) Makkonen, I.; Korhonen, E.; Prozheeva, V.; Tuomisto, F. Identification of vacancy defect complexes in transparent semiconducting oxides ZnO, In_2O_3 and SnO_2. *J. Phys.: Condens. Matter* **2016**, *28*, 224002.

(53) Korhonen, E.; Tuomisto, F.; Bierwagen, O.; Speck, J. S.; Galazka, Z. Compensating vacancy defects in Sn- and Mg-doped In_2O_3. *Phys. Rev. B* **2014**, *90*, 245307.

(54) Varley, J. B.; Peelaers, H.; Janotti, A.; Van de Walle, C. G. Hydrogenated cation vacancies in semiconducting oxides. *J. Phys.: Condens. Matter* **2011**, *23*, 334212.

(55) Uedono, A.; Shimayama, K.; Kiyohara, M.; Chen, Z. Q.; Yamabe, K. Study of oxygen vacancies in SrTiO3 by positron annihilation. *J. Appl. Phys.* **2002**, *92*, 2697−2702.

(56) Zhang, D. H.; Ma, H. L. Scattering mechanisms of charge carriers in transparent conducting oxide films. *Appl. Phys. A* **1996**, *62*, 487−492.

(57) Kim, J. I.; Lee, W.; Hwang, T.; Kim, J.; Lee, S.-Y.; Kang, S.; Choi, H.; Hong, S.; Park, H. H.; Moon, T.; Park, B. Quantitative analyses of damp-heat-induced degradation in transparent conducting oxides. *Sol. Energy Mater. Sol. Cells* **2014**, *122*, 282−286.

(58) Deyu, G. K.; Hunka, J.; Roussel, H.; Brötz, J.; Bellet, D.; Klein, A. Electrical Properties of Low-Temperature Processed Sn-Doped In_2O_3 Thin Films: The Role of Microstructure and Oxygen Content and the Potential of Defect Modulation Doping. *Materials* **2019**, *12*, 2232.

(59) Ellmer, K.; Klein, A.; Rech, B. *Transparent conductive zinc oxide: basics and applications in thin film solar cells*; Springer Science & Business Media: 2007; Vol. *104*, p 59−66.

(60) Pisarkiewicz, T.; Zakrzewska, K.; Leja, E. Scattering of charge carriers in transparent and conducting thin oxide films with a non-parabolic conduction band. *Thin Solid Films* **1989**, *174*, 217−223.

(61) Husein, S.; Stuckelberger, M.; West, B.; Ding, L.; Dauzou, F.; Morales-Masis, M.; Duchamp, M.; Holman, Z.; Bertoni, M. I. Carrier scattering mechanisms limiting mobility in hydrogen-doped indium oxide. *J. Appl. Phys.* **2018**, *123*, 245102.

(62) Liu, C. N.; Ozkaya, B.; Steves, S.; Awakowicz, P.; Grundmeier, G. Combined in situ FTIR-spectroscopic and electrochemical analysis of nanopores in ultra-thin SiO_x-like plasma polymer barrier films. *J. Phys. D: Appl. Phys.* **2013**, *46*, No. 084015.

(63) Ishikawa, K.; Ogawa, H.; Fujimura, S. Contribution of interface roughness to the infrared spectra of thermally grown silicon dioxide films. *J. Appl. Phys.* **1999**, *85*, 4076−4082.

(64) Truong, T. N.; Yan, D.; Samundsett, C.; Basnet, R.; Tebyetekerwa, M.; Li, L.; Kremer, F.; Cuevas, A.; Macdonald, D.; Nguyen, H. T. Hydrogenation of Phosphorus-Doped Polycrystalline Silicon Films for Passivating Contact Solar Cells. *ACS Appl. Mater. Interfaces* **2019**, *11*, 5554−5560.

(65) Mewe, A.; Stodolny, M.; Anker, J.; Lenes, M.; Pagès, X.; Wu, Y.; Tool, K.; Geerligs, B.; Romijn, I. Full wafer size IBC cell with polysilicon passivating contacts. *AIP Conf. Proc AIP Conference Proceedings* **2018**, *1999*, No. 040014.

(66) Zhang, Z.; Liao, M.; Huang, Y.; Guo, X.; Yang, Q.; Wang, Z.; Gao, T.; Shou, C.; Zeng, Y.; Yan, B.; Ye, J. Improvement of Surface Passivation of Tunnel Oxide Passivated Contact Structure by Thermal Annealing in Mixture of Water Vapor and Nitrogen Environment. *Solar RRL* **2019**, *3*, 1900105.

(67) Malmbekk, H.; Vines, L.; Monakhov, E. V.; Svensson, B. G. Electronic states at the interface between indium tin oxide and silicon. *J. Appl. Phys.* **2011**, *110*, No. 074503.

(68) Procel, P.; Xu, H.; Saez, A.; Ruiz-Tobon, C.; Mazzarella, L.; Zhao, Y.; Han, C.; Yang, G.; Zeman, M.; Isabella, O. The role of hetero-interfaces and sub-gap energy states on transport mechanisms in silicon heterojunction solar cells. *Progr. Photovolt.: Res. Appl.* **2020**, 935.

(69) Park, H.; Park, H.; Park, S. J.; Bae, S.; Kim, H.; Yang, J. W.; Hyun, J. Y.; Lee, C. H.; Shin, S. H.; Kang, Y.; Lee, H.-S.; Kim, D. Passivation quality control in poly-Si/SiO /c-Si passivated contact solar cells with 734 mV implied open circuit voltage. *Sol. Energy Mater. Sol. Cells* **2019**, *189*, 21−26.

(70) Feldmann, F.; Bivour, M.; Reichel, C.; Hermle, M.; Glunz, S. W. Passivated rear contacts for high-efficiency n-type Si solar cells providing high interface passivation quality and excellent transport characteristics. *Sol. Energy Mater. Sol. Cells* **2014**, *120*, 270−274.